Molecular Imaging of Extracellular Tumor pH to Reveal Effects of Locoregional Therapy on Liver Cancer Microenvironment

Lynn Jeanette Savic[1,2], Isabel Theresa Schobert[1,2], Dana Peters[1], John J. Walsh[1], Fabian Max Laage-Gaupp[1], Charlie Alexander Hamm[1,2], Nina Tritz[1], Luzie A. Doemel[1,2], MingDe Lin[1,3], Albert Sinusas[1,4], Todd Schlachter[1], James S. Duncan[1,5], Fahmeed Hyder[1], Daniel Coman[1], and Julius Chapiro[1]

ABSTRACT

Purpose: To establish magnetic resonance (MR)–based molecular imaging paradigms for the noninvasive monitoring of extracellular pH (pH_e) as a functional surrogate biomarker for metabolic changes induced by locoregional therapy of liver cancer.

Experimental Design: Thirty-two VX2 tumor-bearing New Zealand white rabbits underwent longitudinal imaging on clinical 3T-MRI and CT scanners before and up to 2 weeks after complete conventional transarterial chemoembolization (cTACE) using ethiodized oil (lipiodol) and doxorubicin. MR-spectroscopic imaging (MRSI) was employed for pH_e mapping. Multiparametric MRI and CT were performed to quantify tumor enhancement, diffusion, and lipiodol coverage of the tumor posttherapy. In addition, incomplete cTACE with reduced chemoembolic doses was applied to mimic undertreatment and exploit pH_e mapping to detect viable tumor residuals. Imaging findings were correlated with histopathologic markers indicative of metabolic state (HIF-1α, GLUT-1, and LAMP-2) and viability (proliferating cell nuclear antigen and terminal deoxynucleotidyl-transferase dUTP nick-end labeling).

Results: Untreated VX2 tumors demonstrated a significantly lower pH_e (6.80 ± 0.09) than liver parenchyma (7.19 ± 0.03, $P < 0.001$). Upregulation of HIF-1α, GLUT-1, and LAMP-2 confirmed a hyperglycolytic tumor phenotype and acidosis. A gradual tumor pH_e increase toward normalization similar to parenchyma was revealed within 2 weeks after complete cTACE, which correlated with decreasing detectability of metabolic markers. In contrast, pH_e mapping after incomplete cTACE indicated both acidic viable residuals and increased tumor pH_e of treated regions. Multimodal imaging revealed durable tumor devascularization immediately after complete cTACE, gradually increasing necrosis, and sustained lipiodol coverage of the tumor.

Conclusions: MRSI-based pH_e mapping can serve as a longitudinal monitoring tool for viable tumors. As most liver tumors are hyperglycolytic creating microenvironmental acidosis, therapy-induced normalization of tumor pH_e may be used as a functional biomarker for positive therapeutic outcome.

Introduction

Hepatocellular carcinoma (HCC) is the fourth most common cause of cancer-related deaths worldwide and the incidence rates continue to rise (1). A large subset of patients with HCC is ineligible for curative treatments (2, 3). In this setting, intra-arterial therapies (IAT) such as oil-based, conventional transarterial chemoembolization (cTACE) are widely applied and guideline-approved mainstay treatments with a potential for down-staging and bridging of patients to resection or transplantation (4, 5). However, the efficacy of such nonsurgical therapies remains limited by individual variations of biological and physiologic characteristics of the tumor microenvironment (TME), which in turn result in highly variable susceptibility to standardized anticancer therapies (6).

Reciprocal interactions between cancer cells and the TME are an overarching theme in the dynamic course of carcinogenesis (6). Specifically, the acidification of the TME subject to the metabolic shift of cancer cells to a hyperglycolytic phenotype is considered a principle feature of tumor aggressiveness and associated with poor survival (6, 7). Synthesis of large amounts of lactate and its transfer into the extracellular space via proton-coupled monocarboxylate transporters lead to a low pH in the surrounding TME, which has been proposed as a metabolic indicator for tumor viability and biomarker for aggressiveness in a variety of neoplasms (8, 9).

The "Warburg effect" describes the increased glucose uptake and oxygen-independent glycolytic rates in cancer cells primarily for energy generation (7, 10). However, further research revealed perpetuated flexibility of metabolic pathways in most cancers, suggesting that enhancing glycolysis and subsequent proton as well as lactate accumulation in the interstitial space primarily serve the purpose of building and preserving a hostile protumorigenic niche (11, 12). Local extracellular acidosis promotes proangiogenic signaling and plays a multifaceted role in immune evasion of cancer cells, the stimulation of proteolytic enzymes driving tumor invasion, and resistance to therapy and thus, serves as an early indicator for disease progression (13–17). Thus, there is a clinical need for noninvasive, quantitative imaging biomarkers that can detect these unfavorable metabolic abnormalities and track them longitudinally over the course of anticancer therapies (18). The objective of this study was to employ multiparametric

[1]Department of Radiology and Biomedical Imaging, Yale School of Medicine, New Haven, Connecticut. [2]Institute of Radiology, Charité - Universitätsmedizin Berlin, corporate member of Freie Universität Berlin, Humboldt-Universität, and Berlin Institute of Health, Berlin, Germany. [3]Visage Imaging, Inc., San Diego, California. [4]Department of Internal Medicine (Cardiology), Yale School of Medicine, New Haven, Connecticut. [5]Department of Biomedical Engineering, Yale School of Engineering and Applied Science, New Haven, Connecticut.

D. Coman and J. Chapiro contributed equally to this article.

Corresponding Author: Julius Chapiro, Yale School of Medicine, The Anlyan Center, N312A, New Haven, CT 06520. Phone: 203-785-2428; Fax: 203-785-3024; E-mail: julius.chapiro@yale.edu

Clin Cancer Res 2020;26:428–38

doi: 10.1158/1078-0432.CCR-19-1702

Translational Relevance

The metabolic shift of cancer cells toward a hyperglycolytic phenotype represents a widely accepted principle of carcinogenesis. The consequent acidification of the tumor microenvironment (TME) due to the proton and lactate output is associated with aggressive tumor growth and potentially facilitates resistance to anticancer therapies, for example, by promoting immunoevasive mechanisms. This translational study utilized multiparametric MRI on clinical scanners to establish noninvasive quantitative characterization of the TME with particular focus on extracellular pH in an orthotopic rabbit tumor model for liver cancer. This novel imaging paradigm was used to longitudinally monitor effects of locoregional therapy and revealed partial normalization of tumor acidosis. The findings establish pH imaging as a functional surrogate biomarker allowing for noninvasive detection and monitoring of viable and metabolically active tumor in the context of cancer therapy. The results suggest that clinical trials investigating applications of pH-mapping in patients with liver cancer should be considered.

imaging paradigms including molecular extracellular pH (pH_e) mapping for TME monitoring in solid liver tumors treated with locoregional therapies. A translational orthotopic animal model for liver cancer was utilized to facilitate clinical translation of the newly developed imaging biomarkers on clinical MRI/CT scanners.

Materials and Methods

VX2 rabbit liver tumor model

Male New Zealand white rabbits (2.5–4 kg, Charles River Laboratories) were used in accordance with institutional guidelines under approved Animal Care and Use Committee protocols. Animals were maintained in laminar flow rooms at constant temperature and humidity, with food and water provided *ad libitum*. Thirty-two rabbits underwent implantation of VX2 tumors in the left lobe of the liver as explained in detail previously (19, 20). Briefly, VX2 tumor chunks were injected into the quadriceps muscle of the hind leg of a donor rabbit and tumors were allowed to grow for 3 weeks. The tumor chunks were harvested from the donor animal and approximately 0.4 mL were injected into the left liver lobe of a recipient rabbit via median laparotomy using a 18G catheter. Abdominal fascias and skin were closed in two layers using absorbable suture materials (chromic gut 3.0; vicryl 4.0). The tumors were allowed to grow for 14 days until a well delineated solitary tumor (1–2.0 cm in diameter) was measurable on CT or MRI (21).

For all surgical interventions, the animals were initially sedated with intramuscular acepromazine 0.25–1 mg/kg and ketamine hydrochloride 30–45 mg/kg. Surgeries and MRI were performed under general anesthesia using isoflurane 1%–3% in oxygen. Supplemental heat support was provided and physiologic monitoring (oxygen saturation, heart rate, and body temperature) was performed during the experiment. Analgesic meloxicam (0.3 mg/kg) and buprenorphine (0.02–0.05 mg/kg) were administered subcutaneously before and after surgical interventions.

Experimental study design

Before tumor induction, animals were randomly assigned to the following five groups with different predetermined endpoints for pH_e mapping and subsequent necropsy and histopathologic evaluation (**Fig. 1**). Hence, pH_e maps were obtained: (i) before treatment (control group; $n = 7$), (ii) immediately (1–2 days; $n = 7$), (iii) 1 week (5–7 days; $n = 7$), or (iv) 2 weeks (14–15 days; $n = 8$) after complete cTACE. In addition, analysis was performed in (v) intentionally undertreated animals ($n = 3$) with pH_e mapping 2 weeks (14 days) posttreatment, as described below. This analysis aimed to elucidate the prognostic value of pH_e imaging to detect tumor residuals in the setting of incomplete cTACE with reduced drug amounts to mimic unsuccessful treatment.

To facilitate interpretation of the created pH_e maps, rabbits also underwent multiparametric MRI (mpMRI) at various time points. All animals underwent baseline imaging before treatment. Rabbits in the control group (group i) had pH_e mapping at baseline and were euthanized afterwards without any treatment. Animals in groups ii and iii underwent multimodal imaging at 1 day or 1 week post-cTACE, respectively, including pH_e imaging and were subsequently sacrificed for radiological–histopathologic analysis at the respective study endpoint. Rabbits in groups iv and v had two follow-up MRI scans at 1 day or 1 week, as well as 2 weeks after cTACE including pH_e mapping at 2 weeks followed by euthanasia and tissue harvest for histopathologic analysis. Furthermore, CT scans were acquired at the same time points when MRI was performed (**Fig. 1**).

cTACE

Lipiodol–doxorubicin emulsion

Doxorubicin HCl (RPI, Mount Prospect) powder was reconstituted with sterile water immediately before intra-arterial injection for a final concentration of 1.25 mg/mL. Administered doses were below maximum animal equivalent doses calculated for a common clinically used doxorubicin dose of 50 mg based on the FDA guidelines for dose translation according to body surface area (22, 23). The doxorubicin solution was mixed thoroughly to obtain a homogenous clear red solution. The solution was mixed 1:2 with lipiodol (Guerbet) using a push-and-pull method with a chemotherapy-resistant plastic stopcock and stable formation of droplets was tested by drop-test (24).

Complete transarterial chemoembolization procedure

Access to the right common femoral artery was gained via blunt dissection and followed by the placement of a 3-French vascular sheath (Cook, Inc.). A 2-French microcatheter (JB1 catheter; Cook, Inc.) was advanced into the celiac axis, after which a celiac arteriogram was acquired to delineate the blood supply to the liver. The tumor was visualized on digital subtraction angiography as a region of hypervascular blush in the left liver lobe. As tumor-feeding vessels nearly exclusively derived from the left hepatic artery, this artery was selectively catheterized off the common hepatic artery using a steerable guide wire (0.014in. Transcend wire; Boston Scientific). Once adequate positioning of the catheter in close proximity to the tumor was confirmed, the mixture of lipiodol and doxorubicin was slowly infused under fluoroscopic guidance. Administered volumes varied between 0.2 mL (doxorubicin dose 0.25 mg) and 0.6 mL (0.75 mg) depending on the tumor size and blood supply. The catheter was cleared with saline followed by 0.3–0.4 mL of 100- to 300-μm beads (Embospheres, Merit Medical) mixed 1:4 with Omnipaque 350 (GE Healthcare) until absence of forward flow in the tumor-supplying artery was observed. Endpoints of embolization were complete administration of lipiodol/doxorubicin suspension and embospheres or premature stagnation of blood flow, as confirmed by intraprocedural fluoroscopy. In addition, multiphasic contrast-enhanced cone-beam (CB) CT images (C-arm; Allura Clarity FD20 8.2; Philips) were acquired intraprocedurally before cTACE to localize the tumor and confirm selective catheter

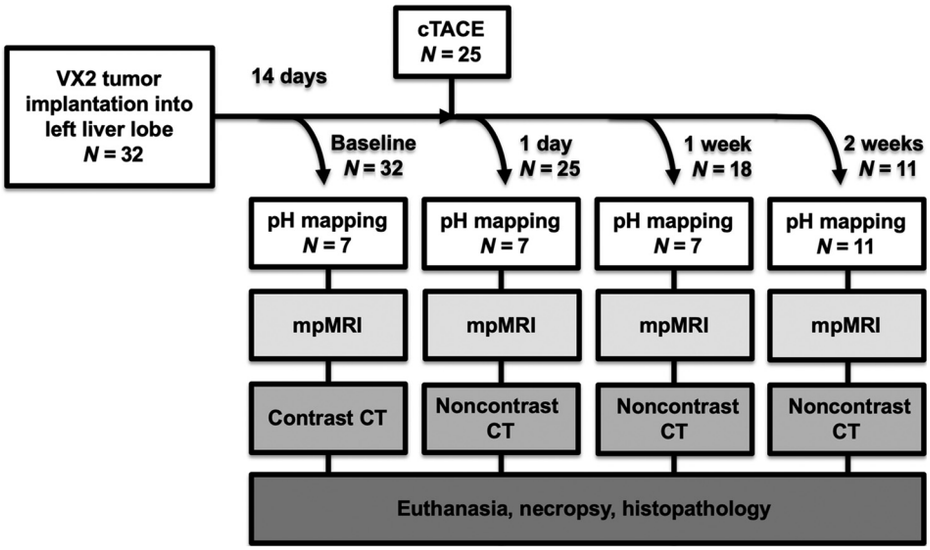

Figure 1.

Experimental *in vivo* study design. In the horizontal direction, the flow chart illustrates the VX2 rabbit tumor model and multimodal imaging at sequential time points. In the vertical, imaging carried out at each time point is displayed according to the respective modality including spectroscopic pH-mapping, mpMRI including contrast-enhanced imaging and ADC-mapping, and CT with or without contrast administration. Briefly, 32 recipient rabbits were implanted into the left liver lobe with tumor chunks harvested from donor rabbits. Tumors were allowed to grow for 2 weeks until baseline imaging was performed. Seven rabbits were euthanized after multimodal imaging at baseline and served as controls. The remaining 25 rabbits were treated with cTACE and received multimodal imaging 1 day later. Seven rabbits were euthanized after each imaging at 1 day and 1 week post-cTACE, respectively, and the remaining rabbits entered the next imaging cycle. A total of 11 rabbits were available for multimodal imaging at 2 weeks post-cTACE. After euthanasia, necropsy was performed and tumor and liver tissue were harvested for radiological–histopathologic comparison.

positioning for improved treatment planning and targeting. Unenhanced CBCT after embolization served to evaluate lipiodol distribution to the tumor. The setting for the CBCT was 120 kVp, 48 cm field of view (FOV), and 305 mAs. Upon completion, the microcatheter was removed, while maintaining gentle suction to avoid expulsion of microspheres remaining in the catheter lumen. The common femoral artery was ligated and the cut-down was closed in two layers using absorbable suture material.

Incomplete transarterial chemoembolization

In addition to complete cTACE, a separate group (v, $n = 3$) was intentionally treated with incomplete embolization to mimic unsuccessful treatment and to elaborate on the prognostic value of pH_e imaging to detect viable tumor residuals in this setting. Incomplete cTACE was performed utilizing substantially reduced doses of lipiodol-doxorubicin emulsion (0.1 mL) and embospheres (0.1 mL). Embolization endpoints for incomplete TACE were defined using intraprocedural CBCT aiming at only partial coverage of the tumor with lipiodol. The intended goal of the intervention was to deliver the defined doses of the agents to reduce patency and perfusion of the tumor-feeding vessels without achieving total stasis, as confirmed on fluoroscopy.

Multimodal imaging and quantitative image analysis

Multiparametric MRI

Chemical shift imaging–pH_e mapping: mpMRI was performed on a 3T-MR unit (Magnetom Prisma; Siemens) marketed for clinical use

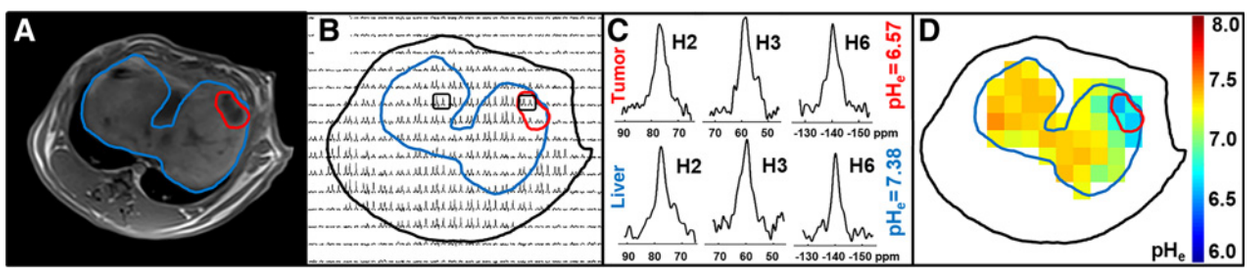

Figure 2.

Spectroscopic noninvasive pH_e mapping using BIRDS. **A,** Axial T_1 VIBE MR images were used for liver (blue) and tumor (red) delineation in a representative untreated VX2 tumor-bearing rabbit. **B,** Distribution of $TmDOTP^{5-}$ peaks from BIRDS with CSI within the tumor and liver are displayed. **C,** Examples of spectra from H2, H3, and H6 protons of $TmDOTP^{5-}$ from a liver and tumor voxel (black squares in **B**) demonstrating the pH_e-dependent chemical shift of the peaks of each proton. **D,** The corresponding pH_e map was calculated using the chemical shifts of H2, H3, and H6 protons of $TmDOTP^{5-}$ in each tumor and liver voxel, respectively, and illustrated with a color map overlay.

with a commercially available 15-channel knee coil. At the time of the respective determined study endpoint, biosensor imaging of redundant deviation in shifts (BIRDS) was performed at the end of the MRI scan to measure pH_e (8, 25). BIRDS combined with the administration of the paramagnetically active contrast agent Thulium (III) 1,4,7,10-Tetraazacyclododecane-1,4,7,10-tetra (TmDOTP; Macrocyclics, Inc.) has been shown to reliably image pH_e by measuring the chemical shift of pH_e sensitive groups of the contrast agent DOTP (8, 25). Briefly, 15-mL $TmDOTP^{5-}$ (0.5 mmol/kg) was infused at 0.5 mL/minute for approximately 30 minutes. The BIRDS data were acquired using a 3D chemical shift imaging (CSI) sequence with a FOV of $20 \times 20 \times 25$ cm, $13 \times 13 \times 13 = 2{,}197$ rectangular encoding steps, a spectral window of 50,000 Hz, 256 complex points with a spectral resolution of 195 Hz/point, TR = 8 ms (limited by specific absorption rate), 6 minutes acquisition time, and reconstructed to $25 \times 25 \times 25$ cm with a voxel resolution of $8 \times 8 \times 10$ mm. Twenty averages were acquired. Water suppression was achieved using a dual-band 640-μs Shinnar-Le Roux RF pulse, which selectively excited the peaks of interest (10 kHz bandwidth) on either side of water. T_1-weighted VIBE images for registration were obtained using a FOV of 20×20 cm, 384×384 matrix, 60 slices, 2.5 mm, TR = 5.2 ms, and TE = 2.5 ms.

As pH_e readouts rely on the chemical shift changes of hyperfine-shifted proton resonances, their molecular sensitivity is independent of the $TmDOTP^{5-}$ concentration without any background overlapping signals. Moreover, BIRDS signals are not affected by the presence of gadolinium-based contrast agents (26, 27).

For postprocessing, the CSI peaks were overlaid on the T_1-weighted images for registration (**Fig. 2**). pH_e was assessed for voxels inside the whole tumor, in the tumor edge consisting of voxels that were adjacent to or 50% outside of the tumor, and outside the tumor in the liver parenchyma. The region of interest (ROI) of normal liver tissue was in general chosen one or two slices ($\geq$10 mm) away from the tumor excluding the gall bladder and central hilus structures. The pH_e for each voxel was calculated from the different dependencies of H2, H3, and H6 chemical shifts of $TmDOTP^{5-}$ using Matlab (MathWorks, Inc.; ref. 25, 28).

Contrast enhanced imaging–tumor enhancement: Tumor enhancement was assessed at all imaging time points on dynamic contrast-enhanced (DCE) T_1-weighted images using a 3D VIBE sequence with CAIPIRINHA (2×2) parallel imaging (29). Scan parameters included: TR/TE/θ = 3.45 ms/1.28 ms/9°, matrix 192×100, 6/8 partial Fourier, bandwidth 500 Hz/pix, FOV = 200×120 mm^2, 25–32 slices, 2–3 s/volume, and $1 \times 2 \times 2.5$ mm^3. Eighty multi-slice volumes were run repeatedly before, during, and after the bolus injection of 0.1 mmol/kg intravenous gadolinium (Dotarem; Guerbet).

Volumetric measurements on the baseline and post-cTACE contrast-enhanced T_1-weighted scans were used to determine the extent of tumor enhancement. Specifically, a quantitative 3D Segmentation Software (IntelliSpace Portalv8, Philips) was applied to segment the total tumor volume (TTV) on the arterial phase (15–20 seconds after contrast administration) based on non-Euclidean geometry and the theory of radial basis function as described in previous work (30). The arterial phase was chosen due to the known hypervascularity of the tumors mainly supplied by hepatic artery branches. Quantitative European Association for the Study of the Liver criteria were applied to calculate the enhancing tumor volume (ETV in cm^3 and % of TTV) as described in detail elsewhere (31). Briefly, the precontrast scan was subtracted from the contrast-enhanced arterial phase images to remove background tissue hyperintensity. A ROI (1 cm^3) was placed in a homogeneous part of liver parenchyma as a subject-specific reference. ETV was defined as voxels where enhancement exceeded two standard deviations (SDs) of the average intensity of the reference ROI (30).

Apparent diffusion coefficient–tumor cellularity: The mpMRI protocol further included respiratory-gated T_2-weighted spin-echo images, unenhanced and contrast-enhanced T_1-weighted Dixon images. Respiratory-gated diffusion-weighted echo-planar imaging (DWI) for reconstruction of apparent diffusion coefficient (ADC) maps utilized three different b values (50–800 s/mm^2) in three orthogonal directions using four scan traces. Scan parameters were: TR/TE/θ/NSA = 2,000 ms/43 ms/9°/4, matrix: 112×112, 6/8 partial Fourier, 92 etl, 1,654 Hz/pix, echo-spacing = 0.71 ms, FOV = 200×160 mm^2, parallel imaging with Grappa ×2, 20 slices, 2.5-mm thickness, 80 mT/m gradients. Fat suppression was applied with spectral attenuation inversion recovery. ADC values reflecting tumor cellularity after cTACE were measured at sequential intervals by means of ROIs placed in the tumor rim and core, and normal liver tissue using ImageJ Software (v1.52a, NIH).

CT imaging–lipiodol coverage

Lipiodol deposition to the tumor is clinically used as a qualitative indicator to assess therapeutic efficacy and correlates with tumor response (32). Multidetector CT scans were acquired using a human-size hybrid 64-slice SPECT/CT Scanner (Discovery 570c, GE Healthcare). Prior to cTACE, unenhanced and triphasic (15 seconds arterial, 70 seconds portal-venous, 5 minutes delayed) contrast-enhanced scans were obtained after intravenous injection of 1 mL/kg Omnipaque 350 at 1 mL/s followed by a saline flush. Other imaging parameters were 120 kVp, 305 mAs, 0.5-mm thickness, and FOV 22×22 cm.

CT post-TACE only comprised unenhanced imaging of the liver for the evaluation of lipiodol deposition. On these native CT scans, lipiodol appeared as hyperdense regions due to its high iodine content. To investigate the role of lipiodol as a tumor-specific imaging marker, the same method used to assess ETV was applied to quantify lipiodol deposition and coverage of the tumor at the various time points (33).

Histopathology

Tissue harvest and processing

Animals were sacrificed by intravenous injection of euthasol (0.5 mL/kg) immediately after MRI with BIRDS at the endpoint required by the study. Tumor and surrounding as well as contralateral liver were immediately harvested, sectioned in slices of 3–5 mm, fixated in 10% buffered formalin overnight, and paraffin-embedded for radiological-histopathologic correlation. In addition, heart, lungs, kidneys, small intestine, colon, stomach, spleen, and muscle were inspected for nontarget lipiodol deposition and treatment toxicity in $n = 3$ animals of each group.

Histopathologic and immunochemistry staining

The tissue was cut into 2-μm slices, deparaffinized using xylene, and rehydrated using a descending ethanol dilution series. After washing with deionized water, samples were permeabilized in boiling retrieval solution for 40 minutes at 95°C. First, hematoxylin and eosin (H&E) stain was used according to standard protocols for general histopathology and quantification of tumor viability and necrosis of all tumors. In addition, IHC was performed on exemplary tumor samples collected for each group. Tumor sections were evaluated for the following targets: HIF-1α (Thermo Fisher Scientific catalog No.

MA1-16504, RRID:AB_568567; 1:20), GLUT-1 (Thermo Fisher Scientific catalog No. PA1-46152, RRID:AB_2302087; 1:200), LAMP-2 (Abcam catalog No. ab13524, RRID:AB_2134736; 1:100), and proliferating cell nuclear antigen (PCNA, Thermo Fisher Scientific catalog No. MA5-11355, RRID:AB_10984046; 1:400 in PBS). Specifically, specimens were incubated with approximately 100 μL of peroxidase quenching solution for 5 minutes and with blocking solution (Invitrogen) for 20 minutes. Incubation with primary antibodies occurred at room temperature in hydration chambers for 50 minutes. Subsequent incubation with biotinylated secondary antibody, streptavidin-peroxidase, and 3,3-diaminobenzidine chromogen was performed as explained previously (34). Hematoxylin was used as a counterstain. Terminal deoxynucleotidyl-transferase dUTP nick-end labeling (TUNEL) was performed using the TUNEL Apoptosis Detection Kit (Millipore catalog No. 17-141) according to the manufacturer's manual.

The histology samples were digitalized and visualized at up to 20 × magnification using Aperio and ImageScope v12.3 Software (Leica Biosystems Imaging, Inc.).

Statistical analysis

A statistical sample size calculation in StatMate 2.0 (GraphPad) was preemptively performed and determined ($n = 7$/group) to be sufficient to detect significant (α, 5%) pH_e differences between group means on the second decimal with high probability (β, 80% power). SDs were estimated on the basis of previous experiments using BIRDS *in vivo* (8). The additional subgroup analysis of incomplete cTACE required $n = 3$ to demonstrate reproducibility of the findings.

All experiments were performed independently and repeated at least three times. Data from the experiments were summarized with means ± SD. Normality testing was performed for each analysis. Statistical comparisons of data sets were evaluated using the unpaired *t* test or Mann–Whitney (two-group comparison) or ANOVA test with Tukey *post hoc* testing or Kruskal–Wallis test (>2 group comparison). Longitudinal measurements were evaluated using the paired Wilcoxon *t* test. Statistical analysis was performed using SPSS (IBM Corp., v24.0) and Prism (v7.0, GraphPad). A two-tailed $P < 0.05$ was considered statistically significant.

Results

Noninvasive pH_e imaging reveals tumor acidosis in a translational animal model of liver cancer

Tumor growth (diameter 1–2 cm) was confirmed on the baseline MRI scan in all animals. In the untreated group, pH_e maps of VX2 tumors indicated a significantly lower pH_e (6.80 ± 0.09) compared with liver tissue ($pH_e = 7.19 \pm 0.03$; $P < 0.001$) revealing acidosis in the tumor. Voxels at the margin of the tumor that were partly outside (>50%) of the T_1-based 3D tumor mask were considered tumor edge. pH_e in the tumor edge ($pH_e = 6.88 \pm 0.07$) was slightly higher than tumor pH_e but still significantly lower than liver parenchyma ($P < 0.001$; **Fig. 3**).

Longitudinal monitoring of pH_e reveals normalization of tumor pH_e in response to cTACE

TACE was technically successful in all 25 animals and embolization endpoints were reached in all animals. However, one animal was observed with lung shunting and lipiodol reflux into more proximal hepatic artery branches during the cTACE procedure. Incomplete embolization was confirmed by patent tumor-feeding artery, incomplete lipiodol coverage of the tumor (<75%), incomplete necrosis, and residual enhancement on postprocedural mpMRI scans as well as histology.

With regards to longitudinal monitoring of therapeutic effects, a steady gradual increase toward pH_e normalization in the tumor and the tumor edge was observed over time at 1 day ($pH_e = 6.85 \pm 0.04$; $P = 0.253$), 1 week ($pH_e = 6.91 \pm 0.04$; $P = 0.002$), and 2 weeks ($pH_e = 7.02 \pm 0.04$; $P < 0.001$) after complete cTACE. However, complete recovery to homeostatic tumor pH_e was not achieved and tumor pH_e remained significantly lower than liver pH_e at all time points. Similar results were observed in the tumor edge.

As opposed to complete cTACE, pH_e mapping 2 weeks after incomplete cTACE indicated regions of both acidic as well as increased, partially neutralized pH_e within the same tumor. Specifically, spatial image registration and comparison of pH_e maps with CT and anatomic mpMRI sequences revealed similarity of the spatial distribution of lipiodol deposition (CT), devascularization (contrast-enhanced T_1), and necrosis (ADC maps) indicative of treated tumor portions with increased tumor pH_e (6.89 ± 0.06) compared with untreated controls. However, this difference was not statistically significant ($P = 0.158$). In contrast, undertreated tumor regions lacking lipiodol deposition appeared as perfused and viable residuals on contrast-enhanced T_1 and ADC maps, respectively. These viable tumor portions revealed acidic tumor pH_e (6.82 ± 0.03) 2 weeks after incomplete cTACE similar to untreated controls ($P = 0.667$). All significant differences between time points are indicated in **Fig. 3**.

Histopathologic characterization of untreated VX2 tumors revealed in the majority of tumors a necrotic tumor core and a viable tumor rim with densely packed tumor cells on H&E stain.

Histopathologic markers indicative of glycolysis (GLUT-1) and chronic acidosis (LAMP-2) were found to be upregulated in untreated VX2 tumors in accordance with pH_e findings. Overexpression of HIF-1α representative of hypoxia was primarily found in tumor cells in proximity to the tumor core. However, expression levels decreased immediately after cTACE and markers were not detectable anymore at 1 and 2 weeks after cTACE along with the onset and increasing extent of tumor necrosis. As opposed to treated tumor regions, histopathologic analysis of undertreated tumor portions after incomplete treatment revealed characteristic viable tumor features with overexpression of HIF-1α, GLUT-2, and LAMP-2.

Evolution of multiparametric imaging biomarkers indicates devascularization, necrosis, and sustained lipiodol coverage post-cTACE

To help interpreting the pH_e results, longitudinal therapeutic effects of cTACE on tumor enhancement and diffusion as well as lipiodol coverage of the tumor were volumetrically quantified on MRI and CT. Mean ETV was 70.89% ± 17.41% at baseline, demonstrating hypervascularity of untreated VX2 tumors. Hyperenhancement was predominant in the tumor rim and mostly absent in the necrotic core. ETV significantly decreased as early as 1 day after cTACE (1.18% ± 1.59%; $P < 0.001$) indicative of devascularization of the tumors that persisted at 1 week (6.03% ± 13.36%; $P < 0.001$) and 2 weeks after cTACE (2.76% ± 3.45%; $P = 0.008$). Volumetric analysis of the whole lesion in purposefully undertreated tumors revealed remaining tumor enhancement within the undertreated portion of the tumor at 2 weeks post-cTACE ($P = 0.006$; **Fig. 4**).

With regards to DWI, untreated tumors demonstrated lower ADC values in the viable tumor rim (857.3 ± 147.1 mm^2/s) compared with liver parenchyma (1,102 ± 76.42 mm^2/s) reflecting high cellular density of the tumor rim ($P < 0.001$). ADC values measured in necrotic

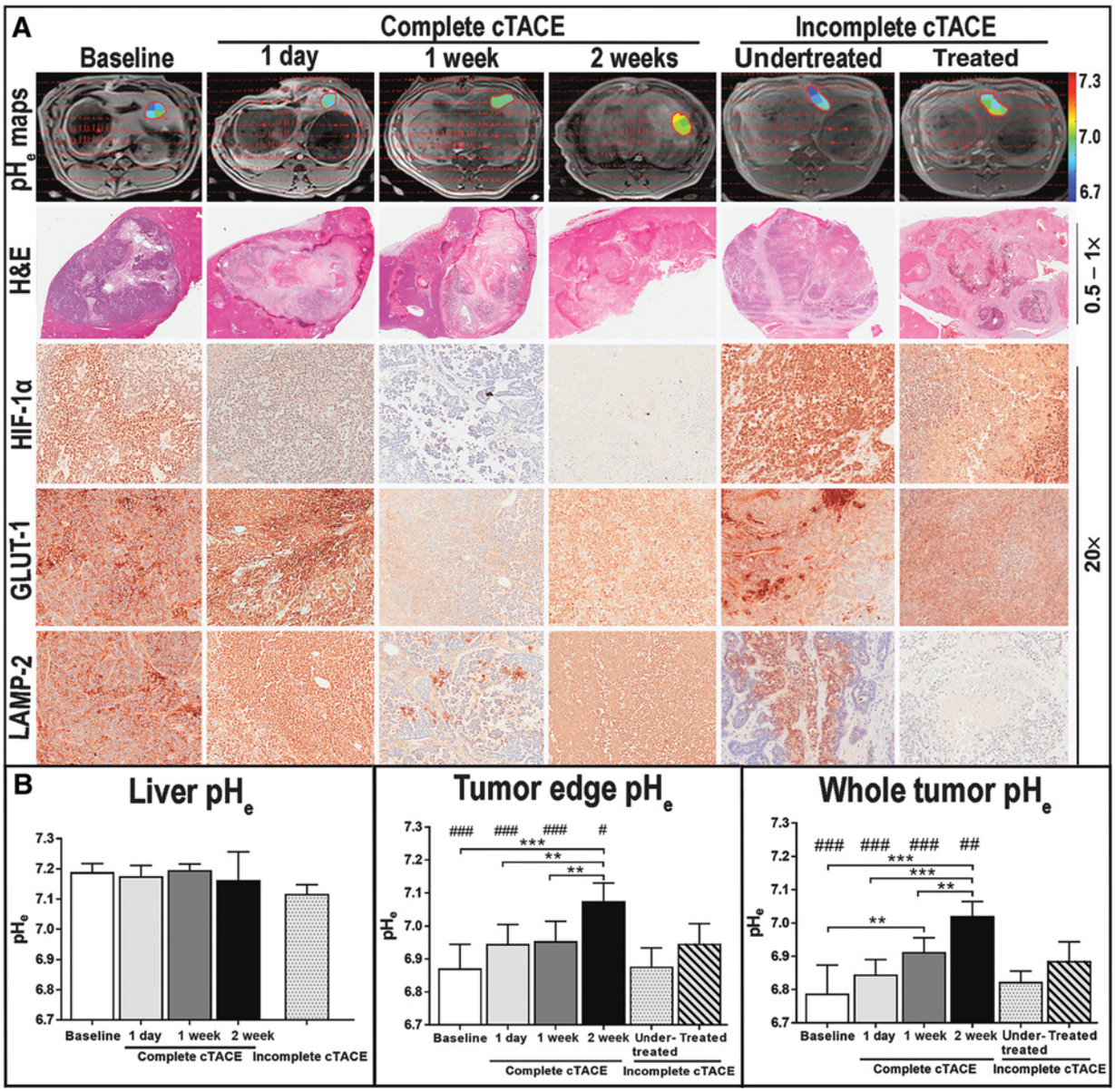

Figure 3.

Evolution of pH_e in liver cancer after cTACE. **A,** In the horizontal direction, images are arranged according to the time of acquisition in relation to the cTACE treatment. In the first row, CSI peaks are shown in red for each voxel, overlaid on the corresponding anatomic T_1 VIBE MR images. Mean pH_e of the example tumors shown in this figure were 6.77 ± 0.03 (control), 6.85 ± 0.02 (1 day), 6.94 ± 0.01 (1 week), 7.05 ± 0.01 (2 weeks), 6.81 ± 0.0 (undertreated), and 6.95 ± 0.03 (treated after incomplete cTACE). VX2 tumors are outlined in red with color map overlays illustrating tumor pH_e. Imaging findings were confirmed on histology of the tumor using H&E, HIF-1α, GLUT-1, and LAMP-2. Control tumors demonstrated a necrotic core and a viable rim with densely packed tumor cells and high expression levels of all metabolic targets, while they were nearly undetectable at 1 day and not detectable at 1 and 2 weeks post-cTACE. pH_e 2 weeks after incomplete cTACE indicated acidosis of undertreated regions determined as viable residuals on anatomic imaging and histology. In addition, treated regions in the same tumor revealed increased pH_e, which corresponded to disappearance of histological markers. **B,** Quantification of pH_e demonstrated significantly lower pH_e in the tumor and tumor edge compared with normal liver in animals that did not undergo cTACE. Longitudinal measurements revealed a gradual increase toward pH_e normalization in the tumor and the tumor edge at 1 day, 1 week, and 2 weeks post-cTACE, although a complete recovery to normalized pH_e was not achieved within this time frame. In normal liver, pH_e values remained stable at all time points. Significant differences are indicated by * between different time points (**, $P < 0.01$; ***, $P < 0.001$) and by # when compared with liver parenchyma at the same respective time point (#, $P < 0.05$; ##, $P < 0.01$; ###, $P < 0.001$).

tumor cores (1,235.08 ± 239.77 mm^2/s) were significantly higher compared with parenchyma ($P = 0.007$) and the tumor rim ($P < 0.001$).

In completely embolized tumors, tumor rim and core were not distinguishable as histologically distinct separate regions. Significant onset of necrosis became apparent immediately after cTACE compared with baseline (1,659.74 ± 555.32 mm^2/s; $P = 0.003$ at 1 day). Extents of necrosis continued to increase at 1 week (2,087.47 ± 530.47 mm^2/s; $P < 0.001$) while remaining stable 2 weeks post-cTACE

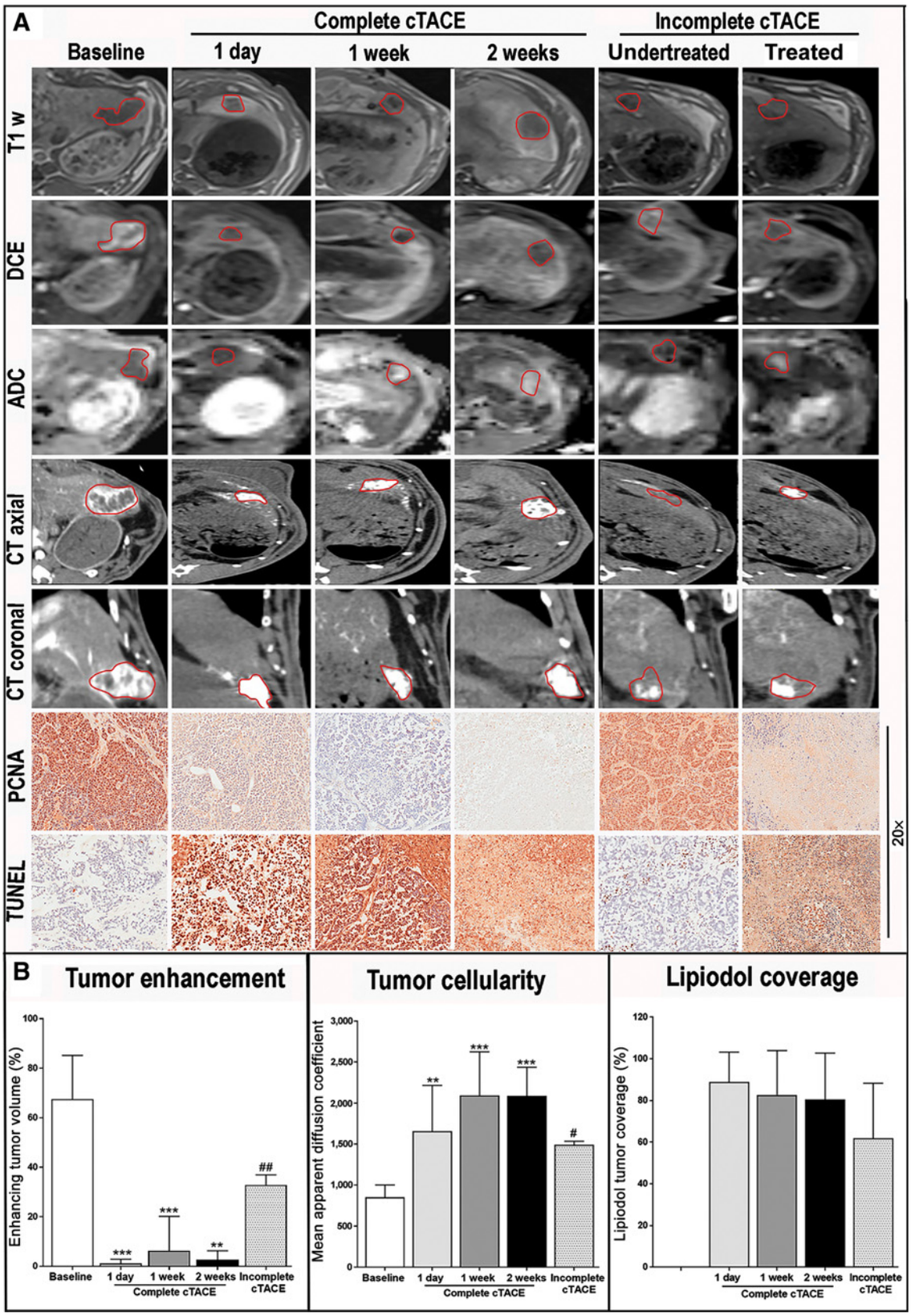

(2,075.53 ± 349.86 mm^2/s; $P < 0.001$), suggesting a loss of tumor cell integrity. Cellularity of liver parenchyma indicated by ADC remained unchanged over time.

Undertreated lesions demonstrated significantly lower ADC values than completely treated tumors at 2 weeks post-TACE indicative of incomplete tumor necrosis (1,625.04 ± 305.37 mm^2/s; $P = 0.012$; **Fig. 4**).

In addition, lipiodol coverage of tumors expressed as percentage of the TTV was >80% 1 day after complete cTACE. Persistent deposition of lipiodol in the tumors across all time points was measured in 27 of 28 animals. Lipiodol deposition was mainly visible in the rim of the tumor and mostly absent in the tumor core. This observation is consistent with the enhancement pattern and ADC maps. The animal observed with lipiodol reflux during the cTACE procedure demonstrated a marked decrease of tumor lipiodol coverage on the 1-week follow-up CT. In the liver parenchyma, gradual and ultimately near-complete wash-out of nontarget lipiodol deposition was observed until 2 weeks post-cTACE. Undertreated tumors after incomplete cTACE showed a lower total lipiodol coverage of 67.53% ± 26.37% as compared to completely treated tumors.

The multiparametric imaging findings were histopathologically confirmed by H&E as well as PCNA and TUNEL stainings. The control group showed substantial PCNA staining in the viable tumor rim, whereas the inner core did not stain with PCNA indicating necrosis. TUNEL, as a marker for apoptosis and cell death, highlighted the inner core and did not stain the viable tumor rim in the control group complementing the negative PCNA staining. Post-cTACE, H&E staining showed broader necrosis radiating from the core in the treated tumors at 1 day post-cTACE compared with the control tumors and increasing extents of necrosis over time. In animals sacrificed 1 or 2 weeks after cTACE, areas of necrosis exceeded the margins of the tumor affecting surrounding liver tissue. At all time points post-cTACE, no distinct PCNA staining could be observed within the tumor and TUNEL staining was visible throughout the entire tumor. On the contrary, undertreated tumors after incomplete cTACE demonstrated histologic features of control tumors in viable residual tumor regions adjacent to necrotic, treated portions (**Fig. 4**).

Discussion

This study established MR-spectroscopic noninvasive pH_e mapping, in addition to MRI and CT parameters, as a monitoring strategy for therapeutic efficacy of locoregional therapy of liver cancer. Most liver tumors exhibit a hyperglycolytic metabolic phenotype that results in the extracellular accumulation of lactate and protons and thus, acidification of the TME (35, 36). Therefore, the main finding of this study shows experimental evidence that therapy-induced interruption of tumor metabolism leads to normalization of tumor pH_e. This paradigm can then be used as a functional molecular imaging biomarker for longitudinal monitoring of therapeutic outcome after nonsurgical treatments of liver cancer.

Molecular imaging in this rabbit liver cancer model revealed acidic tumor pH_e in viable, untreated tumors that was significantly lower than pH_e measured in healthy liver parenchyma. There is ample evidence supporting that extracellular tumor acidity and lactic acidosis are important tumor-extrinsic components of tumor formation and progression as they stimulate neoangiogenesis and facilitate local tumor invasion (13, 14). Low pH_e further contributes to an immunosuppressive environment via quiescence of cellular antitumoral immune response and thus, promotes immunoevasion of cancer cells (9, 15, 16). However, tumor metabolism and the mode of nutrient acquisition in cancer cells need to adapt to changing nutrient- and oxygen-poor microenvironments (37). These conditions may vary significantly resulting in heterogeneity of metabolic phenotypes across tumor types, as well as in distinct regions within the same tumor (38, 39). Thus, the ability for noninvasive pH_e imaging of TME acidification may help develop better understanding of the underlying tumor biology and monitor individual metabolic activity to predict susceptibility prior to anticancer therapies and tumor response after treatment. On a molecular level, the low tumor pH_e results from alterations of the expression levels of metabolic proteins such as GLUT-1 in untreated tumors (36). In addition, this study utilized a newly established histologic marker LAMP-2 for pathologic correlation with *in vivo* pH_e mapping, whose translocation and expression on cell membranes is associated with chronic acidosis in cancer cells (**Fig. 3**) (40).

Monitoring of the metabolic activity of liver tumors is particularly challenging given the high metabolic activity of liver parenchyma, which is likely to cause unspecific background signal, as often observed in positron emission tomography with fluorodeoxyglucose (41). Contrary to many fluorescent, luminescent, or radioactive probes, MR-spectroscopic imaging constitutes a noninvasive radiation-free approach to quantify functional cancer characteristics that can go beyond morphologic feature assessment (18, 42–44). MR-based approaches already available for clinical use include hyperpolarized MRI measuring metabolic flux and chemical exchange saturation transfer (CEST). CEST is a pH-sensitive technique that measures the chemical exchange between endogenous compounds (i.e., proteins, amino acids, and sugars) and bulk water (45). Although CEST provides MRI capability at slightly higher resolution than BIRDS, it lacks specificity due to overlapping signals from exchangeable groups (i.e., –NH and –OH). Moreover, CEST is not fully quantitative due to several confounding factors such as temperature or magnetic field inhomogeneities, although some of these confounders can be accounted for (46). In comparison, pH_e mapping with BIRDS does not depend on temperature or agent concentration. BIRDS has been validated previously in rat brains at 9.4T using 31-phosphorus MRS. However, as these validations are based purely on chemical shift

Figure 4.

Evolution of multimodal multiparametric imaging biomarkers in liver cancer after cTACE. **A,** The figure illustrates representative changes of liver tumors on mpMRI and CT induced by cTACE. In the vertical direction, the imaging scans are arranged according to the time of acquisition. In the horizontal, images are arranged according to the modality including precontrast T_1-weighted (T_{1w}) images, DCE images in the arterial phase (15–20 seconds after contrast bolus injection), and ADC maps, all in axial plane, and axial as well as coronal CT images with (baseline) and without (post-cTACE) contrast administration. Untreated tumors demonstrated rim hyperenhancement on contrast-enhanced MRI and CT and a viable tumor rim (low ADC) and necrotic core (high ADC). Corresponding histology from the tumor rim revealed strong ubiquitous staining with the proliferation marker PCNA and low signal from TUNEL staining of cell death. Treatment with cTACE achieved durable devascularization and onset of necrosis as early as 1 day post-cTACE and sustained lipiodol deposition at all time points. These findings were histologically confirmed by disappearance of PCNA signal and high TUNEL signal in tumors post-cTACE. **B,** Box plots from volumetric quantification of arterial tumor enhancement (DCE), tumor cellularity (ADC), and lipiodol coverage (CT) of the tumor illustrate the longitudinal cTACE effects. Significant differences are indicated by * compared with baseline (**, $P < 0.01$; ***, $P < 0.001$) and by # for comparison of incomplete cTACE with complete cTACE both at 2 weeks after treatment (#, $P < 0.05$; ##, $P < 0.01$).

regardless of the amplitude or frequency of the $TmDOTP^{5-}$ peaks, they should be independent of magnetic field strength and thus, valid at 3T as well. The fast relaxing MR-signals allow for rapid data acquisition with increased averaging and thus, improved signal-to-noise ratio (SNR). In addition, due to the broad MR resonances of $TMDOPT^{5-}$, BIRDS is less sensitive to magnetic field inhomogeneities.

This study demonstrates the feasibility of BIRDS on clinical 3T-MR scanners. The pH_e measurement on a voxel-by-voxel basis with inherent spatial information allows to account for heterogeneities within examined tissues. Besides the capability of quantifying pH_e in untreated tumors with high reproducibility (low SD within groups), molecular pH_e mapping proved sensitive to detect small changes of tumor pH_e upon treatment with cTACE. Locoregional therapy of liver tumors achieved a gradual reduction of tumor acidosis with increasing pH_e values toward the pH_e of normal liver parenchyma. Each pH_e mapping was followed by tumor harvest and histopathologic cross-validation of imaging findings. Moreover, to help establish tumor pH_e as a new biomarker, mpMRI was applied to assess treatment efficacy to full extent using readily clinically available sequences and inform interpretation of tumor pH_e measurements in the same model. While devascularization and tumor necrosis became visible on MRI as early as 1 day after treatment and remained largely unchanged over time, evolution of functional pH_e changes of the tumor were explicitly measurable by BIRDS, reflecting the typical gradual pathologic response to cTACE, which was undetectable by conventional mpMRI. These findings suggest a high sensitivity of the pH_e mapping to monitor longitudinal physiologic changes over time.

In clinical patients, tumor recurrence after cTACE is fairly common due to technical challenges, as well as unknown susceptibility of individual tumors to a certain treatment (47). Therefore, it is clinically desirable to identify recurrence early after cTACE and improve patient management by developing personalized treatment strategies. The mechanism of cTACE is a synergistic effect of chemotherapy and embolization-induced depletion of oxygen and nutrients (4). We hypothesize that cTACE will initially result in decreased glycolysis and thus, reduced amounts of lactate and protons being secreted into the extracellular space in the TME. This "shut-down" of the "Warburg effect" will become measurable as an increase in pH_e, as detected by BIRDS in this study. This hypothesis is further supported by the findings in the incomplete cTACE group, which mimics the clinical scenario of treatment failure. Remarkably, imaging of tumor pH_e after incomplete cTACE revealed low pH_e values 2 weeks post-cTACE in tumor regions without lipiodol deposits that appeared as viable residuals on contrast-enhanced MRI and ADC maps as well as histology. Adjacent to those viable portions, successfully treated regions became apparent on MRI showing no enhancement and high ADC values indicative of necrosis. Those treated tumor regions corresponded to increased pH_e as compared with baseline. These results underscore the potential to exploit pH_e imaging as a sensitive indicator for tumor viability and a surrogate marker for tumor susceptibility and response to anticancer therapies that result in normalization of tumor pH_e.

The newly discovered capacity of cTACE to neutralize tumor acidosis and reestablish pH_e homoeostasis in the liver, bears significant potential to enrich therapeutic possibilities by combination with other treatments in the management of liver cancer. Specifically, targeting the tumor stroma by dissolving tumor acidity may lower the barrier of immunosuppression and facilitate both intrinsic antitumoral immune response as well as implementation of immuno-therapies for liver cancer. Thus, this set of instruments to monitor pH_e may further advance the development of targeted approaches to disrupt resistance mechanisms that currently hamper the efficacy of locoregional and combination treatments with the ultimate goal to improve clinical outcome.

One of the limitations of this study was the relatively low spatial resolution of the CSI voxels, which could potentially be improved in future studies by increasing the SNR using a more sensitive coil and more efficient k-space sampling methods. In addition, while gating in anesthetized rabbits may not be necessary given the relatively small chest movement (<3 mm) compared with the voxel size, awake experiments may require respiratory gating but would come at a price of reduced temporal resolution. Moreover, point-spread function correction should be integrated to prevent distortion and incorrect reconstruction of the acquired MR data. Despite the steady gradual increase of pH_e over time, no complete normalization of tumor pH_e was reached in this study. Hence, further analyses may include longer follow-up windows to elucidate long-term effects of cTACE on tumor pH_e and the prognostic value of possible pH_e decrease with tumor recurrence. However, the findings after intentional incomplete embolization to mimic the clinical scenario of treatment failure underscore the predictive value of pH_e to detect viable tumor residuals based on tumor acidity. Furthermore, the study was conducted on VX2 tumors of nonhepatic origin in the absence of a cirrhotic liver background. However, VX2 tumors are a common model for the study of liver cancer and previously reported results involving cTACE have been rather predictive of clinical outcomes (48). They demonstrate a growth pattern reminiscent of locally destructive and metastatic tumors, which has been used to model various cancer entities and the hypervascularity and relatively large vessels mimic the imaging appearance of HCC and are suitable to employ IATs such as cTACE (49). Most importantly, VX2 tumors represent a hyperglycolytic phenotype with prominent "Warburg effect", which is exploited for imaging of peritumoral acidification in this study (19, 50). The model also overcomes inherent problems of frequently used rodent models and allows for cTACE therapy according to clinical standards and universally applicable imaging sequences on state-of-the-art 3T-MRI scanners. Although pharmacokinetic studies in rat models demonstrated renal clearance of $TmDOTP^{5-}$, they also revealed a subordinate slow equilibrating space with slow release of $TmDOTP^{5-}$ presumably from bone (51). Therefore, future studies should include dedicated safety assessments for the use of $TmDOTP^{5-}$ in the rabbit tumor model to further pave the way for clinical translation.

In conclusion, this translational study established and validated noninvasive quantitative imaging of tumor pH_e as a novel molecular surrogate biomarker for tumor metabolism and viability in liver cancer and implemented pH_e mapping to reveal therapeutic efficacy of cTACE. As the acidification of the TME normalizes throughout the course of successful therapy, the results strengthen the role of pH_e for the functional monitoring of tumor response to cTACE. These findings provide a novel conceptual framework for imaging-based noninvasive metabolic profiling of liver cancer that can be exploited as an organizing principle for personalized treatment strategies.

Disclosure of Potential Conflicts of Interest

No potential conflicts of interest were disclosed by the authors.

Authors' Contributions

Conception and design: L.J. Savic, D. Peters, M. Lin, T. Schlachter, J.S. Duncan, F. Hyder, D. Coman, J. Chapiro

Development of methodology: L.J. Savic, D. Peters, J.J. Walsh, M. Lin, A. Sinusas, T. Schlachter, J.S. Duncan, F. Hyder, D. Coman, J. Chapiro

Acquisition of data (provided animals, acquired and managed patients, provided facilities, etc.): L.J. Savic, I.T. Schobert, D. Peters, J.J. Walsh, F.M. Laage-Gaupp, C.A. Hamm, N. Tritz, L.A. Doemel, M. Lin, A. Sinusas, F. Hyder, D. Coman, J. Chapiro

Analysis and interpretation of data (e.g., statistical analysis, biostatistics, computational analysis): L.J. Savic, I.T. Schobert, D. Peters, C.A. Hamm, M. Lin, J.S. Duncan, F. Hyder, D. Coman, J. Chapiro

Writing, review, and/or revision of the manuscript: L.J. Savic, I.T. Schobert, D. Peters, J.J. Walsh, C.A. Hamm, N. Tritz, M. Lin, A. Sinusas, T. Schlachter, J.S. Duncan, F. Hyder, D. Coman, J. Chapiro

Administrative, technical, or material support (i.e., reporting or organizing data, constructing databases): L.J. Savic, I.T. Schobert, C.A. Hamm, N. Tritz, L.A. Doemel, M. Lin, F. Hyder, J. Chapiro

Study supervision: L.J. Savic, D. Peters, T. Schlachter, F. Hyder, D. Coman, J. Chapiro

Acknowledgments

This study was funded by the NIH (R01 CA206180 and R01 EB023366) and the Society of Interventional Oncology (19-001324). Research reported in this article was also supported by the Yale Liver Center Microscopy Core of the NIDDK under award number P30KD034989. L.J. Savic reports receiving grants from Leopoldina Post-doctoral Fellowship outside the submitted work. J. Chapiro reports receiving grants from the German-Israeli Foundation for Scientific Research and Development, The Rolf W. Günther Foundation for Radiological Research, Boston Scientific/BTG, Philips Healthcare, and Guerbet outside the submitted work. M. Lin is a Visage Imaging employee. I.T. Schobert reports receiving grants from the Biomedical Education Program outside the submitted work. The authors would like to thank Boston Scientific and Guerbet for providing expendable supplies and materials for the experimental part of the study. We also thank Christi Hawley, Marina Mammarian, Stephanie Thorn, Lucas Adam, Sophie Antonia Stark, Paula Oestmann, Jonathan Tefera, and Bing Liu for their support in animal care and handling.

The costs of publication of this article were defrayed in part by the payment of page charges. This article must therefore be hereby marked *advertisement* in accordance with 18 U.S.C. Section 1734 solely to indicate this fact.

Received May 30, 2019; revised July 24, 2019; accepted September 30, 2019; published first October 3, 2019.

References

1. Bray F, Ferlay J, Soerjomataram I, Siegel RL, Torre LA, Jemal A. Global cancer statistics 2018: GLOBOCAN estimates of incidence and mortality worldwide for 36 cancers in 185 countries. CA Cancer J Clin 2018;68:394–424.
2. Fong ZV, Tanabe KK. The clinical management of hepatocellular carcinoma in the United States, Europe, and Asia: a comprehensive and evidence-based comparison and review. Cancer 2014;120:2824–38.
3. Lintoiu-Ursut B, Tulin A, Constantinoiu S. Recurrence after hepatic resection in colorectal cancer liver metastasis -review article. J Med Life 2015;8:12–4.
4. European Association For The Study Of The Liver, European Organisation For Research and Treatment Of Cancer. EASL-EORTC clinical practice guidelines: management of hepatocellular carcinoma. J Hepatol 2012;56: 908–43.
5. Lencioni R, de Baere T, Soulen MC, Rilling WS, Geschwind JF. Lipiodol transarterial chemoembolization for hepatocellular carcinoma: a systematic review of efficacy and safety data. Hepatology 2016;64:106–16.
6. Hanahan D, Weinberg RA. Hallmarks of cancer: the next generation. Cell 2011; 144:646–74.
7. Warburg O. On respiratory impairment in cancer cells. Science 1956;124:269–70.
8. Coman D, Huang Y, Rao JU, De Feyter HM, Rothman DL, Juchem C, et al. Imaging the intratumoral-peritumoral extracellular pH gradient of gliomas. NMR Biomed 2016;29:309–19.
9. Damaghi M, Gillies R. Phenotypic changes of acid-adapted cancer cells push them toward aggressiveness in their evolution in the tumor microenvironment. Cell Cycle 2017;16:1739–43.
10. Lunt SY, Vander Heiden MG. Aerobic glycolysis: meeting the metabolic requirements of cell proliferation. Annu Rev Cell Dev Biol 2011;27:441–64.
11. Schwartz L, Seyfried T, Alfarouk KO, Da Veiga Moreira J, Fais S. Out of Warburg effect: an effective cancer treatment targeting the tumor specific metabolism and dysregulated pH. Semin Cancer Biol 2017;43:134–8.
12. Denko NC. Hypoxia, HIF1 and glucose metabolism in the solid tumour. Nat Rev Cancer 2008;8:705–13.
13. Vegran F, Boidot R, Michiels C, Sonveaux P, Feron O. Lactate influx through the endothelial cell monocarboxylate transporter MCT1 supports an NF-B/IL-8 pathway that drives tumor angiogenesis. Cancer Res 2011;71:2550–60.
14. Rofstad EK, Mathiesen B, Kindem K, Galappathi K. Acidic extracellular pH promotes experimental metastasis of human melanoma cells in athymic nude mice. Cancer Res 2006;66:6699–707.
15. Fischer K, Hoffmann P, Voelkl S, Meidenbauer N, Ammer J, Edinger M, et al. Inhibitory effect of tumor cell-derived lactic acid on human T cells. Blood 2007; 109:3812–9.
16. Goetze K, Walenta S, Ksiazkiewicz M, Kunz-Schughart LA, Mueller-Klieser W. Lactate enhances motility of tumor cells and inhibits monocyte migration and cytokine release. Int J Oncol 2011;39:453–63.
17. Moellering RE, Black KC, Krishnamurty C, Baggett BK, Stafford P, Rain M, et al. Acid treatment of melanoma cells selects for invasive phenotypes. Clin Exp Metastasis 2008;25:411–25.
18. Anemone A, Consolino L, Arena F, Capozza M, Longo DL. Imaging tumor acidosis: a survey of the available techniques for mapping *in vivo* tumor pH. Cancer Metastasis Rev 2019;38:25–49.
19. Hong K, Khwaja A, Liapi E, Torbenson MS, Georgiades CS, Geschwind JF. New intra-arterial drug delivery system for the treatment of liver cancer: preclinical assessment in a rabbit model of liver cancer. Clin Cancer Res 2006; 12:2563–7.
20. Buijs M, Vossen JA, Geschwind JF, Salibi N, Pan L, Ventura VP, et al. Quantitative proton MR spectroscopy as a biomarker of tumor necrosis in the rabbit VX2 liver tumor. J Vasc Interv Radiol 2011;22:1175–80.
21. Hong K, Kobeiter H, Georgiades CS, Torbenson MS, Geschwind JF. Effects of the type of embolization particles on carboplatin concentration in liver tumors after transcatheter arterial chemoembolization in a rabbit model of liver cancer. J Vasc Interv Radiol 2005;16:1711–7.
22. Reagan-Shaw S, Nihal M, Ahmad N. Dose translation from animal to human studies revisited. FASEB J 2008;22:659–61.
23. Andrade EL, Bento AF, Cavalli J, Oliveira SK, Schwanke RC, Siqueira JM, et al. Non-clinical studies in the process of new drug development - part II: good laboratory practice, metabolism, pharmacokinetics, safety and dose translation to clinical studies. Braz J Med Biol Res 2016;49:e5646.
24. de Baere T, Zhang X, Aubert B, Harry G, Lagrange C, Ropers J, et al. Quantification of tumor uptake of iodized oils and emulsions of iodized oils: experimental study. Radiology 1996;201:731–5.
25. Coman D, Trubel HK, Rycyna RE, Hyder F. Brain temperature and pH measured by (1)H chemical shift imaging of a thulium agent. NMR Biomed 2009;22:229–39.
26. Maritim S, Huang Y, Coman D, Hyder F. Characterization of a lanthanide complex encapsulated with MRI contrast agents into liposomes for biosensor imaging of redundant deviation in shifts (BIRDS). J Biol Inorg Chem 2014;19: 1385–98.
27. Huang Y, Coman D, Herman P, Rao JU, Maritim S, Hyder F. Towards longitudinal mapping of extracellular pH in gliomas. NMR Biomed 2016;29: 1364–72.
28. Coman D, Peters D, Walsh JJ, Savic LJ, Huber S, Sinusas AJ, et al. Extracellular pH mapping of liver cancer on a clinical 3T MRI scanner. Magn Reson Med 2019; DOI: 10.1002/mrm.28035.
29. Michaely HJ, Morelli JN, Budjan J, Riffel P, Nickel D, Kroeker R, et al. CAIPIRINHA-Dixon-TWIST (CDT)-volume-interpolated breath-hold examination (VIBE): a new technique for fast time-resolved dynamic 3-dimensional imaging of the abdomen with high spatial resolution. Invest Radiol 2013;48:590–7.
30. Chapiro J, Wood LD, Lin M, Duran R, Cornish T, Lesage D, et al. Radiologic-pathologic analysis of contrast-enhanced and diffusion-weighted MR imaging in patients with HCC after TACE: diagnostic accuracy of 3D quantitative image analysis. Radiology 2014;273:746–58.
31. Lin M, Pellerin O, Bhagat N, Rao PP, Loffroy R, Ardon R, et al. Quantitative and volumetric European association for the study of the liver and response

evaluation criteria in solid tumors measurements: feasibility of a semiautomated software method to assess tumor response after transcatheter arterial chemoembolization. J Vasc Interv Radiol 2012;23:1629–37.
32. Chen CS, Li FK, Guo CY, Xiao JC, Hu HT, Cheng HT, et al. Tumor vascularity and lipiodol deposition as early radiological markers for predicting risk of disease progression in patients with unresectable hepatocellular carcinoma after transarterial chemoembolization. Oncotarget 2016;7:7241–52.
33. Chen R, Geschwind J-F, Wang Z, Tacher V, Lin M. Quantitative assessment of lipiodol deposition after chemoembolization: comparison between cone-beam CT and multidetector CT. J Vasc Interv Radiol 2013;24:1837–44.
34. Chapiro J, Sur S, Savic LJ, Ganapathy-Kanniappan S, Reyes J, Duran R, et al. Systemic delivery of microencapsulated 3-bromopyruvate for the therapy of pancreatic cancer. Clin Cancer Res 2014;20:6406–17.
35. Macheda ML, Rogers S, Best JD. Molecular and cellular regulation of glucose transporter (GLUT) proteins in cancer. J Cell Physiol 2005;202:654–62.
36. DeBerardinis RJ, Lum JJ, Hatzivassiliou G, Thompson CB. The biology of cancer: metabolic reprogramming fuels cell growth and proliferation. Cell Metab 2008;7:11–20.
37. Tomaszewski W, Sanchez-Perez L, Gajewski TF, Sampson JH. Brain tumor microenvironment and host state - implications for immunotherapy. Clin Cancer Res 2019;25:4202–10.
38. Longo DL, Bartoli A, Consolino L, Bardini P, Arena F, Schwaiger M, et al. *In vivo* imaging of tumor metabolism and acidosis by combining PET and MRI-CEST pH imaging. Cancer Res 2016;76:6463.
39. Hensley CT, Faubert B, Yuan Q, Lev-Cohain N, Jin E, Kim J, et al. Metabolic heterogeneity in human lung tumors. Cell 2016;164:681–94.
40. Damaghi M, Tafreshi NK, Lloyd MC, Sprung R, Estrella V, Wojtkowiak JW, et al. Chronic acidosis in the tumour microenvironment selects for overexpression of LAMP2 in the plasma membrane. Nat Commun 2015;6:8752.
41. Cho Y, Lee DH, Lee YB, Lee M, Yoo JJ, Choi WM, et al. Does 18F-FDG positron emission tomography-computed tomography have a role in initial staging of hepatocellular carcinoma? PLoS One 2014;9:e105679.
42. Wyatt LC, Lewis JS, Andreev OA, Reshetnyak YK, Engelman DM. Applications of pHLIP technology for cancer imaging and therapy. Trends Biotechnol 2017;35:653–64.
43. Peeters SG, Zegers CM, Lieuwes NG, van Elmpt W, Eriksson J, van Dongen GA, et al. A comparative study of the hypoxia PET tracers [^{18}F]HX4, [^{18}F]FAZA, and [^{18}F]FMISO in a preclinical tumor model. Int J Radiat Oncol Biol Phys 2015;91:351–9.
44. Haris M, Yadav SK, Rizwan A, Singh A, Wang E, Hariharan H, et al. Molecular magnetic resonance imaging in cancer. J Transl Med 2015;13:313.
45. Hancu I, Dixon WT, Woods M, Vinogradov E, Sherry AD, Lenkinski RE. CEST and PARACEST MR contrast agents. Acta Radiol 2010;51:910–23.
46. Kim J, Wu Y, Guo Y, Zheng H, Sun PZ. A review of optimization and quantification techniques for chemical exchange saturation transfer MRI toward sensitive *in vivo* imaging. Contrast Media Mol Imaging 2015;10:163–78.
47. Lencioni R. Loco-regional treatment of hepatocellular carcinoma. Hepatology 2010;52:762–73.
48. Mostafa EM, Ganguli S, Faintuch S, Mertyna P, Goldberg SN. Optimal strategies for combining transcatheter arterial chemoembolization and radiofrequency ablation in rabbit VX2 hepatic tumors. J Vasc Interv Radiol 2008;19:1740–8.
49. Parvinian A, Casadaban LC, Gaba RC. Development, growth, propagation, and angiographic utilization of the rabbit VX2 model of liver cancer: a pictorial primer and "how to" guide. Diagn Interv Radiol 2014;20:335–40.
50. Shope RE, Hurst EW. Infectious papillomatosis of rabbits: with a note on the histopathology. J Exp Med 1933;58:607–24.
51. Makos JD, Malloy CR, Sherry AD. Distribution of TmDOTP5- in rat tissues: TmDOTP5- vs. CoEDTA- as markers of extracellular tissue space. J Appl Physiol 1998;85:1800–5.